Primljen / Received: 11.1.2025.
Ispravljen / Corrected: 10.5.2025.
Prihvaćen / Accepted: 2.6.2025.
Dostupno online / Available online: 10.11.2025.

Seismic performance of partially encased composite joints

Authors:

[1,2]Prof. **Hongxin Liu**
Liuhx@aisa.com.cn

[2]**Bing Xia**, MCE
bing_xia@arcplus.com.cn

[1,2]**Yaming Li**, MCE
Liym@aisa.com.cn

[1,2]**Shuizhong Jia**, MCE
Jiasz@aisa.com.cn

[3]**Xiaomeng Xie**, PhD. CE
xiexiaomeng2024@163.com
Corresponding author

[1] Shanghai Institute of Architectural Design and Research d.o.o., China
[2] Shanghai Spatial Structure Engineering Research Center, China
[3] Construction Technology Shanghai Jieyi, China

Original research paper

Hongxin Liu, Bing Xia, Yaming Li , Shuizhong Jia, Xiaomeng Xie

Seismic performance of partially encased composite joints

To evaluate the seismic performance of partially encased composite (PEC) joints with different connection configurations, quasi-static loading tests were performed on two PEC joint specimens. The experimental investigation focused on the failure mechanisms, hysteresis characteristics, ductility, energy dissipation capacity, and stiffness degradation under low-cycle repeated loading. The results revealed that strong-axis PEC joints exhibited superior ductility and energy-dissipation capacity, whereas weak-axis joints experienced weld failure and demonstrated limited energy dissipation. A finite element model was developed for strong-axis PEC joints and validated using experimental data. Moreover, the restoring force model for strong-axis PEC joints accurately captured the hysteretic behavior, providing valuable insights for structural design applications.

Key words:
PEC beam-column joints, seismic performance, energy dissipation, finite element analysis, restoring model

Izvorni znanstveni rad

Hongxin Liu, Bing Xia, Yaming Li , Shuizhong Jia, Xiaomeng Xie

Seizmička svojstva djelomično ovijenih spregnutih spojeva

Kako bi se ocijenila seizmička otpornost djelomično ovijenih spregnutih (eng. *partially encased composite* - PEC) spojeva s priključcima različitih konfiguracija, provedena su kvazistatička ispitivanja na dvama ispitnim uzorcima PEC spojeva. Eksperimentalna istraživanja bila su usmjerena na mehanizme loma, histerezna svojstva, duktilnost, sposobnost trošenja energije i smanjenje krutosti pri cikličkome opterećivanju s malim brojem ciklusa. Dobiveni rezultati pokazali su da djelomično ovijeni spregnuti spojevi s djelovanjem opterećenja u smjeru jake osi ostvaruju bolju duktilnost i veću sposobnost trošenja energije, dok su spojevi u smjeru slabe osi doživjeli lom zavara i pokazali ograničenu sposobnost trošenja energije. Razvijen je model konačnih elemenata za PEC spojeve duž jake osi i potvrđen primjenom eksperimentalnih podataka. Osim toga razvijeni model povratne sile vjerno prikazuje histerezno ponašanje spojeva, što omogućuje njihovu učinkovitu primjenu u projektiranju nosivih konstrukcija.

Ključne riječi:
PEC spojevi grede i stupa, seizmičko ponašanje, trošenje energije, metoda konačnih elemenata, model povrata

1. Introduction

Prefabricated reinforced concrete structures have been widely adopted because of their notable advantages in terms of construction efficiency, resource conservation, and quality control [1]. However, these structures still encounter several challenges, including difficulties in reinforcing the joint core, inadequate concrete vibration performance, loose grouting in the sleeves, and excessive wet work, all of which significantly hinder the industrialization of the construction sector [2, 3]. Partially encased composite (PEC) structures, which represent a novel form of composite construction, are created by embedding shear connectors within the steel flanges and pouring concrete, thereby reducing the construction complexity while maintaining superior structural performance [4]. Extensive studies on PEC beams [5, 6] and columns [7, 8] have demonstrated that the concrete encased within the steel flanges substantially enhances the structural stiffness and fire resistance, whereas shear connectors effectively mitigate local flange buckling, ultimately improving the load-bearing capacity, ductility, and energy-dissipation capability of PEC components. Moreover, various innovative PEC configurations, including honeycomb and perforated web PEC beams [9, 10], L-shaped PEC columns [11], and corrugated web PEC columns [12], have exhibited promising mechanical performance.

Joints serve as critical components that connect beams and columns in a structure [13]. They experience a combination of compressive, bending, and shear forces when subjected to external loads, making them key locations for structural failure or collapse, particularly during earthquakes [14]. Consequently, their mechanical performance directly influences the overall safety and reliability of the structure. Pekgokgoz et al. [15] demonstrated that incorporating steel-fiber-reinforced concrete into beam-to-column joints significantly enhanced their ductility, with the most pronounced fiber-reinforcement effect observed at a 1 % volume ratio. De Souza Spavier et al. [16] investigated the mechanical performance of PEC column-to-steel beam joints using end plates and bolts, and concluded that this connection type is safe and reliable, with concrete contributing significantly to the stiffness and moment capacity of the joints [17, 18]. Huang et al. [19, 20] designed and tested frame specimens featuring steel hollow PEC beams, revealing failure modes similar to those of conventional steel beam frames but with superior initial lateral stiffness, ultimate bearing capacity, and energy-dissipation capacity. Yu et al. [21] conducted quasi-static loading tests on a 1/3-scale two-story two-span PEC column steel plate shear wall (SPSW) structure incorporating three types of semi-rigid connections. Their findings indicated that the proposed PEC-SPSW system exhibited excellent seismic performance, effectively leveraging the shear capacity of the PEC columns to establish a dual lateral resistance system. PEC joints offer notable advantages in terms of seismic performance and prefabrication efficiency, reducing onsite labor and construction costs. Further investigation of their restoring force models would facilitate broader applications in practical engineering.

The restoring force model serves as a fundamental tool for seismic analysis because its curve variations reflect the constitutive behavior of the material model and are influenced by multiple factors, including the axial load ratio, concrete confinement, and sectional configuration of the structure [22-24]. Yang et al. [25] proposed a trilinear skeleton curve model for modular steel-concrete composite columns, detailing the stiffness degradation and hysteretic behavior, and validated the reliability of the model through experimental testing. Zhuang et al. [26] conducted low-cycle repeated load tests on three types of mechanically connected prefabricated beam-column joints, fitting the unloading-reloading paths to determine the inflection points, clamping points, unloading stiffness, and reloading stiffness in the hysteresis curves. Their findings led to the development of an effective load model that incorporated slip and clamping effects. Wu et al. [27] developed a restoring force model for modular prefabricated steel plate concrete column H steel beam composite joints and demonstrated its high accuracy through finite element comparisons. Dai et al. [28] collected experimental data from 77 corroded and 26 uncorroded rectangular reinforced concrete columns subjected to cyclic loading and established a phenomenological hysteretic model for corroded reinforced concrete columns. In conclusion, an optimal restoring force model can capture the structural response under seismic loading more accurately, thereby facilitating improved seismic design and analysis [29].

Most research in this field to date has focused on the component level, such as PEC beams and PEC columns, whereas investigations of PEC joints primarily focus on PEC column-to-steel beam connections. However, relatively limited research has been conducted on PEC beam-column joints. To address this gap, this study designed half-scale PEC beam-column joints and conducted low-cycle repeated loading tests to examine their mechanical behavior and failure modes under strong- and weak-axis connections. The analysis included hysteresis curves, skeleton curves, ductility performance, strength degradation, stiffness degradation, and energy-dissipation capacity, with the aim of comprehensively evaluating the seismic performance of PEC beam-column joints. Furthermore, a restoring force model for strong-axis PEC joints was developed using finite element analysis, thereby providing a theoretical foundation for the dynamic time-history analysis of strong-axis PEC joints.

2. Experimental program

2.1. Specimen design

This experiment was conducted as part of the Shanghai World Expo Cultural Park Twin Hills Landscape Project, which represents the largest domestic application of PEC structures. All structural components used in the Twin Hills project were large-section PEC members. In this study, two

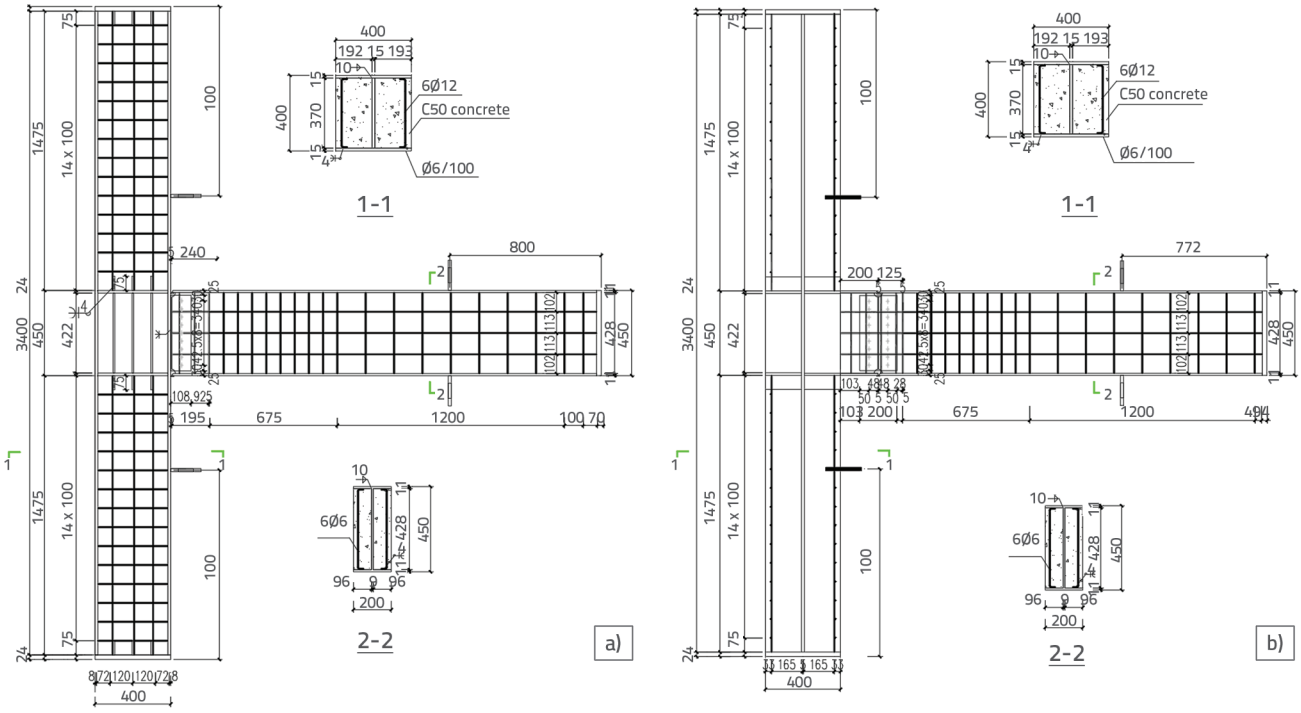

Figure 1. Schematic of PEC joints: a) J-1; b) J-2

large-section PEC beam-column joint specimens, labeled J-1 and J-2, were designed at a 0.5 scale. The primary steel components of the beams and columns were fabricated from Q355B grade steel. The column sections measured H400 × 400 × 15 × 9 mm, with a total height of 3400 mm. The cross braces within the columns were constructed using HRB400 grade steel bars with a diameter of 6 mm and spacing of 100 mm. The beam sections had dimensions of H200 × 450 × 11 × 9 mm and a total length of 4500 mm. The cross braces in the beams were also made of HRB400 grade steel bars, with a diameter of 8 mm and spacing of 200 mm, while in the densified zone, the spacing was reduced to 100 mm, with three C6 horizontal distribution bars arranged on each side. In the joint region, the thicknesses of the transverse and longitudinal stiffening ribs were 14 and 10 mm, respectively. The concrete used in the specimens was grade C50. Specimen J-1 represented a strong-axis connection, where the PEC beam was connected along the strong axis of the PEC column, corresponding to the web direction of its H-shaped steel section. In this configuration, the primary loading direction of the beam aligns with the strong axis of the column, resulting in greater overall joint stiffness, which enables the joint to withstand higher bending moments and shear forces. Conversely, specimen J-2 represented a weak-axis connection, where the PEC beam was connected along the weak axis of the PEC column, corresponding to the flange direction of its H-shaped steel section. Because the primary loading direction of the beam aligns with the weak axis of the column, the joint exhibits lower stiffness and relatively weaker flexural resistance. In this configuration, the load-bearing capacity is primarily governed by the stiffness of the column flanges. A detailed schematic of the specimen construction is shown in Figure 1.

2.2. Material property tests

Both the PEC beams and columns were cast using C50 commercial concrete. During specimen fabrication, 150 mm edge-length cubic samples were reserved to measure the compressive strength f_{cu} of the concrete after standard curing. The material property tests for the concrete were conducted at the Building Materials Laboratory of Tongji University, in accordance with the national Standard for Test Methods of Physical and Mechanical Properties of Concrete (GB/T50081-2019) [30]. The failure mode of the concrete specimens is illustrated in Figure 2, whereas the measured compressive strengths of the cubic specimens are presented in Table 2.

The material properties of the steel were evaluated in accordance with the national standard Metallic Materials - Tensile Testing (GB/T 228.1-2010) [31]. Standard tensile tests were conducted using a universal testing machine in the Structural Engineering Laboratory at Tongji University. The loading apparatus is illustrated in Figure 3. All of the steel plates used in the specimens were sourced from the same batch and cut into proportional samples for testing. The yield strength fy, ultimate strength fu, and elastic modulus E of the steel materials with varying thicknesses are summarized in Table 2.

Table 1. Strength values of concrete

Number	f_{cu} [MPa]		f_c [MPa]	f_c average value [MPa]	E_c [GPa]
	Experimental value	Average value			
1-1	57.9	56.4	36.5	37.8	35.6
1-2	55.4				
1-3	56.0				
2-1	60.9	60.3	39.0		
2-2	59.5				
2-3	60.6				

Table 2. Material properties of steel

Strength class	t [mm]	f_y [MPa]	f_u [MPa]	E [MPa]
Q355B	10	446.8	560.5	217696
	12	360.6	512.9	213275
	14	359.7	536.4	206843

Figure 2. Failure pattern of concrete standard test block

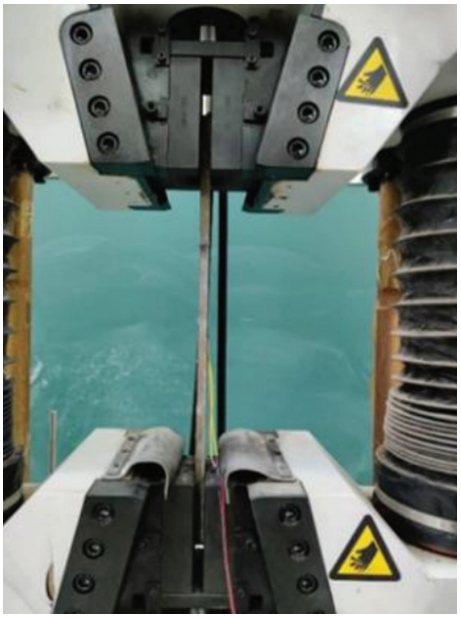

Figure 3. Loading of steel standard specimens

2.3. Loading Protocol and measurement

A force-displacement dual-control loading protocol was adopted according to the Code for Seismic Test Methods of Buildings (JGJ101-96) [32]. In this protocol, horizontal forces and displacements were applied at the column ends using horizontal actuators, as illustrated in Figure 4.

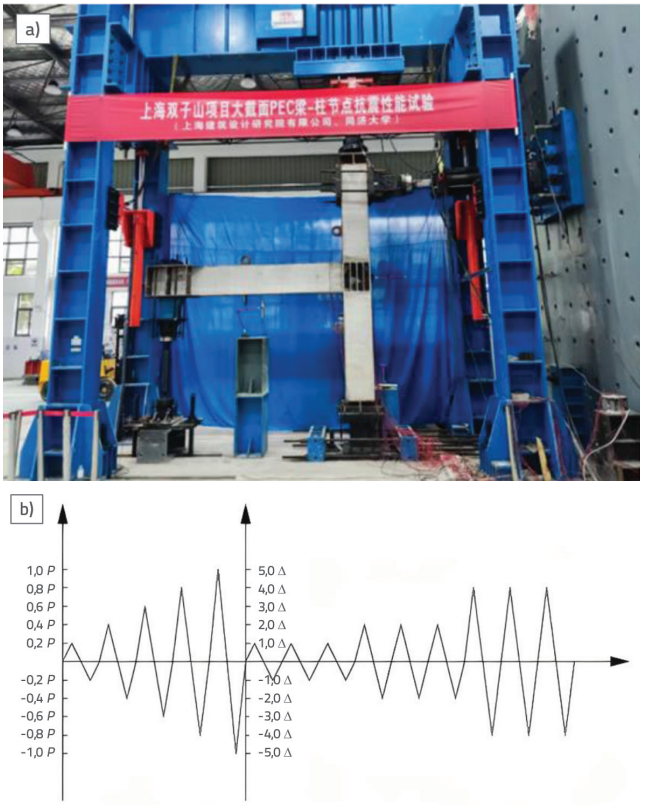

Figure 4. Test loading: a) Loading device; b) Specimen loading system

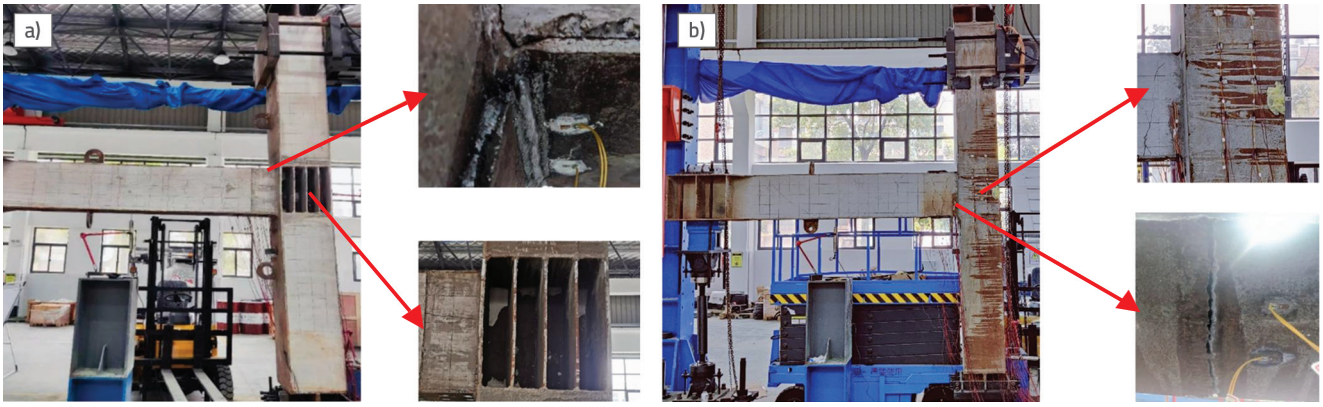

Figure 5. Failure modes of PEC joints: a) Failure mode of specimen J-1; b) Failure mode of specimen J-2

During the load-controlled phase, prior to reaching the yield load, the specimen was subjected to incremental loading in small deformation stages under load control, and the calculated yield load was denoted as P. The load was divided into five levels: 0.2P, 0.4P, 0.6P, 0.8P, and P, with each level applied incrementally and repeated once. Based on the material property test results, the loading continued until the steel yielded. In the displacement-controlled phase, upon reaching the yield load, displacement control was implemented using the horizontal displacement corresponding to the yield load (Δ, the yield displacement) as the initial displacement level. Loading was then carried out in increments of 1Δ, 2Δ, 3Δ, 4Δ, 5Δ, etc., with each level cycled three times, until the specimen was completely destroyed; that is, when its bearing capacity decreased to 85 % of the peak load.

3. Experimental results analysis

3.1. Experimental phenomena

The actual positive yield load of the strong-axis PEC beam-column joint (specimen J-1) was 98.36 kN, with a positive yield displacement of 30.44 mm and positive peak load of 111.70 kN. Similarly, the actual yield load of the weak-axis PEC beam-column joint (specimen J-2) was 95.64 kN, with a yield displacement of 34.68 mm and peak load of 101.00 kN.

Specimen J-1 entered a cracked working state after reaching 0.6 Py. Vertical and diagonal micro-cracks first appeared on both beam surfaces. When the load reached 1.0 Py, the column flange started to bend, accompanied by abnormal noises, and minor concrete spalling was observed on the compressed side at the root of the beam. At this stage, the top and bottom flanges of the PEC beam reached yield strain. At 1.0Δ, the maximum crack width in the beam increased to 0.94 mm, while a new diagonal crack with a maximum crack width of 0.25 mm appeared in the column. At 3.0Δ, the strain in the top and bottom flanges of the PEC beam continued to increase, leading to significant concrete cracking and slight deformation of the core steel. During negative loading at 3.0Δ, the bearing capacity of the specimen dropped below 85 % of its ultimate load, at which point the test was terminated.

Specimen J-2 entered a cracked working state after reaching 0.4Py. Vertical and diagonal micro-cracks first appeared on both beam surfaces. When the load reached 1.0Py, the column flange started to bend, and the top flange of the PEC beam reached yield strain. At this stage, J-2 completed the load-controlled phase and transitioned to the displacement-controlled phase. The horizontal displacement corresponding to the yield load, denoted as Δ, was taken as the initial displacement level. At 1.0Δ, the weld at the beam end fractured, causing a sudden drop in load, and the test was subsequently terminated. At this point, the maximum crack width in the concrete was measured as 0.26 mm. The final failure modes of the specimens are illustrated in Figure 5.

3.2. Hysteresis and skeleton curves

The load and displacement values at the column end under low-cycle repeated loading were recorded, and the corresponding load-displacement hysteresis curves are shown in Figure 6(a). The skeleton curves, which were constructed by connecting the peak points of the load-displacement curves from the first loading cycle at each level, are shown in Figure 6.b.

The actual positive yield load of specimen J-1 was 98.4 kN, with a corresponding positive yield displacement of 30.4 mm. The positive peak load reached 111.7 kN, occurring at a displacement of 51.1 mm. The ultimate positive load was recorded as 94.9 kN, with an associated ultimate displacement of 101.9 mm, yielding a ductility coefficient of 3.35. In the negative loading direction, the actual yield load of specimen J-1 was 141.4 kN, with a negative yield displacement of 40.3 mm. The peak negative load reached 143.1 kN at a displacement of 53.7 mm. The ultimate negative load was 121.6 kN, with an ultimate displacement of 156.5 mm, and the calculated ductility coefficient was 3.89.

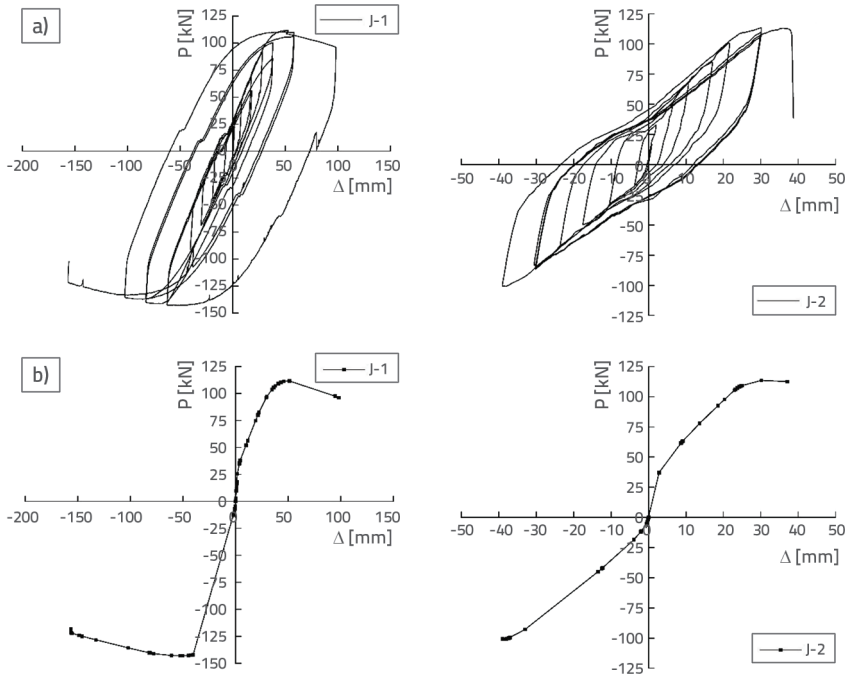

Figure 6. Hysteresis and skeleton curves of specimen: a) Hysteresis curve; b) Skeleton curve

The actual positive yield load for specimen J-2 was 101.0 kN, with a corresponding positive yield displacement of 21.4 mm. The positive peak load reached 113.6 kN at a displacement of 30.2 mm. The ultimate positive load was recorded as 96.6 kN, with an ultimate positive displacement of 30.2 mm, yielding a ductility coefficient of 1.41. In the negative loading direction, the actual yield load of specimen J-2 was 95.6 kN, with a negative yield displacement of 34.7 mm. The peak negative load reached 101.0 kN at a displacement of 38.2 mm. The ultimate negative load was 85.9 kN, with an ultimate displacement of 70.0 mm, and the calculated ductility coefficient was 3.03.

The skeleton curves of the specimens exhibited an approximately S-shaped pattern, indicating that the joints experienced three distinct loading stages throughout the test: elastic, elastoplastic, and failure. In the initial loading stage, the joints sustained minor damage, and the load-bearing capacity and deformation maintained a linear relationship, with the stiffness remaining almost constant, corresponding to the straight segment of the skeleton curve. As the loading progressed, the damage gradually accumulated and the steel flanges of the beam and column near the joints started to yield. This led to a reduction in the slope of the skeleton curve, indicating a decrease in stiffness. After reaching the ultimate load-bearing capacity, the skeleton curve transitioned to a descending phase, reflecting the maximum accumulation of structural damage. At this stage, concrete spalling became evident, deformation increased sharply, and the load-bearing capacity decreased, ultimately resulting in negative stiffness and joint failure. For specimen J-2, failure occurred at the weld at the beam end after reaching the ultimate load-bearing capacity, leading to a loss of the reverse load-bearing capacity. However, the skeleton curve did not exhibit the characteristic descending segment observed in the other cases.

The load-displacement values corresponding to the yield, peak, and ultimate limit points of the specimens are summarized in Table 3. Specimen J-1 exhibited higher yield and peak loads compared with specimen J-2. This difference can be attributed to the failure mechanism of specimen J-2, in which the weld between the corbel and beam fractured at a relatively exterior location, resulting in a slightly lower final load-bearing capacity than that of specimen J-1. The ductility coefficient of specimen J-1 exceeded 3, demonstrating good ductility performance of the strong-axis PEC joint. In contrast, specimen J-2 exhibited a significantly smaller ductility coefficient of approximately 1.13. This reduced ductility was primarily owing to the short corbel design of the column, which positioned the weld too close to the beam end. Consequently, weld failure occurred prematurely, preventing the joint from exhibiting effective energy dissipation.

3.3. Energy-consuming capacity

In practical engineering structures, a higher equivalent viscous damping coefficient and greater cumulative energy dissipation indicate improved energy dissipation

Table 3. Summary of feature point parameters

Sample code	Positive (+) and negative (-) load	Yield point		Peak point		Ultimate point		Ductility factor $\mu = \Delta_u / \Delta_y$
		P_y [kN]	Δ_y [mm]	P_{maks} [kN]	Δ_{maks} [mm]	P_u [kN]	Δ_u [mm]	
J-1	+	98.36	30.44	111.70	51.06	94.94	101.86	3.35
	-	141.42	40.26	143.10	52.69	121.64	156.52	3.89
J-2	+	100.98	21.44	113.60	30.16	96.56	37.13	1.73
	-	95.64	34.68	101.00	38.21	85.85	39.05	1.13

performance. Theequivalent viscous damping coefficient he was calculated based on Figure 7 and Equation (1). The equivalent viscous damping coefficients and cumulative energy dissipation values of the specimens are shown in Figure 8.

$$h_e = \frac{1}{2\pi}\frac{(S_{ABC}+S_{ACF})}{(S_{OBD}+S_{OEF})} \quad (1)$$

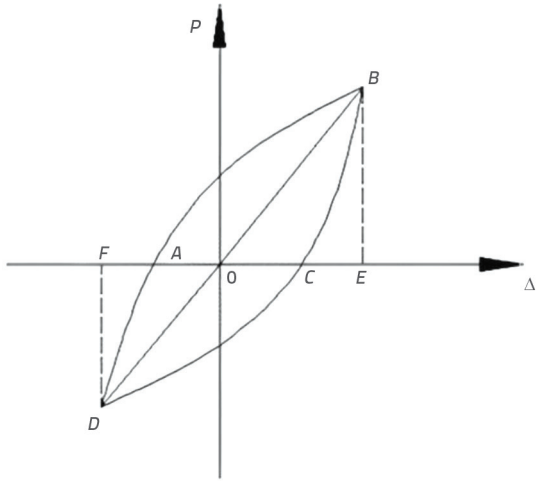

Figure 7. Equivalent viscous damping coefficient and calculation diagram

As shown in Figure 8, after the joints fully entered the plastic stage, they continued to exhibit high cumulative energy dissipation and equivalent viscous damping coefficients. This indicates that the specimens maintained substantial energy-dissipation capacity even after reaching their ultimate load-bearing capacity. These findings demonstrate that PEC joints exhibit excellent seismic performance.

3.4. Stiffness degradation

The stiffness degradation of the two specimens was analyzed using the secant stiffness method, as outlined in the Code for Seismic Test Methods of Buildings [30]. The calculation method for the secant stiffness K is provided in Equation (2) and the corresponding results are illustrated in Figure 9.

$$K_i = \frac{|+F_i|+|-F_i|}{|+X_i|+|-X_i|} \quad (2)$$

where F_i is the i load peak value [kN], and X_i is the peak of the i displacement [mm].

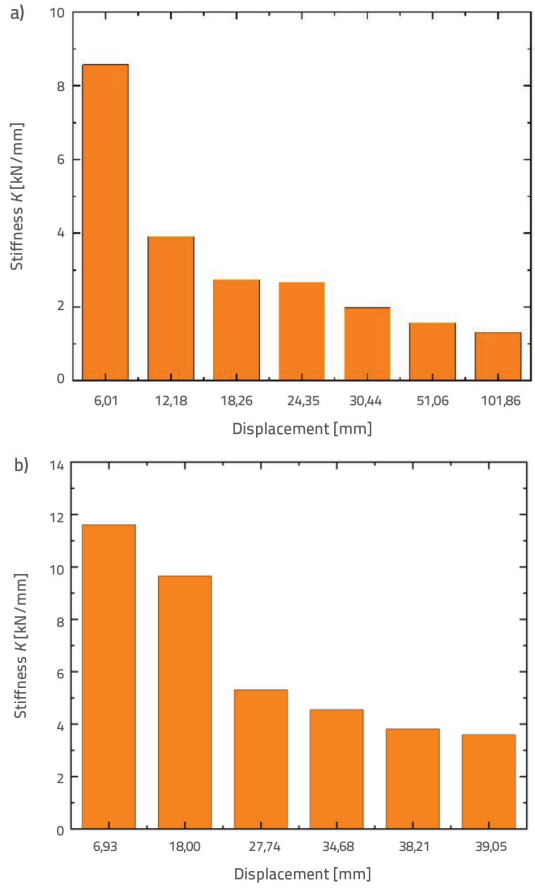

Figure 9. Rigidity degeneration: a) Specimen J-1; b) Specimen J-2

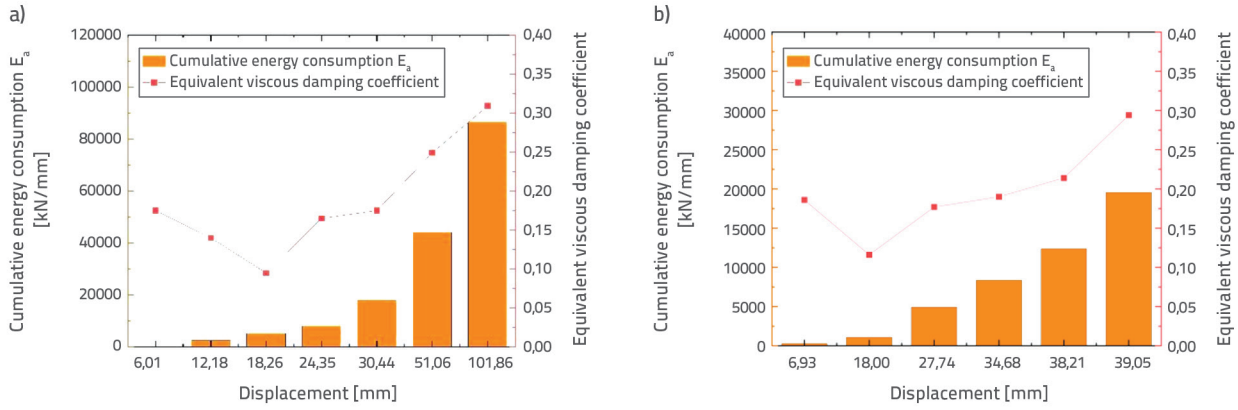

Figure 8. Equivalent viscous damping coefficient and cumulative energy dissipation of joints: a) Specimen J-1; b) Specimen J-2

In the initial loading stage, the joints remained in the elastic phase, and their stiffness degraded rapidly upon crack formation. As the cyclic loading progressed, the damage accumulated continuously, causing the rate of load increase to slow significantly compared with the displacement increase, which in turn led to more gradual stiffness degradation. During the later loading stages, the stiffness of the joints remained low, indicating a high degree of structural damage.

4. Finite element analysis of strong-axis PEC joints

According to the above test analysis results, the performance of specimen J-1 with a strong-axis connection was superior to that of specimen J-2 with a weak-axis connection in all aspects. Therefore, further finite element analysis was performed to investigate the behavior of PEC joints with strong-axis connections.

4.1. Finite element modeling

A numerical model was developed in ABAQUS to simulate the failure process of the strong-axis PEC joints under quasi-static loading. This model incorporates various geometric components and force interactions, utilizing two-node three-dimensional truss elements (T3D2) for the steel reinforcement and links, whereas the concrete and steel beams are represented using eight-node three-dimensional solid hexahedral reduced integration elements (C3D8R). A structured mesh technique with a uniform element size of 100 mm was applied to the steel, concrete, links, longitudinal reinforcement, and construction steel. The details of the mesh partitioning are presented in Figure 10.

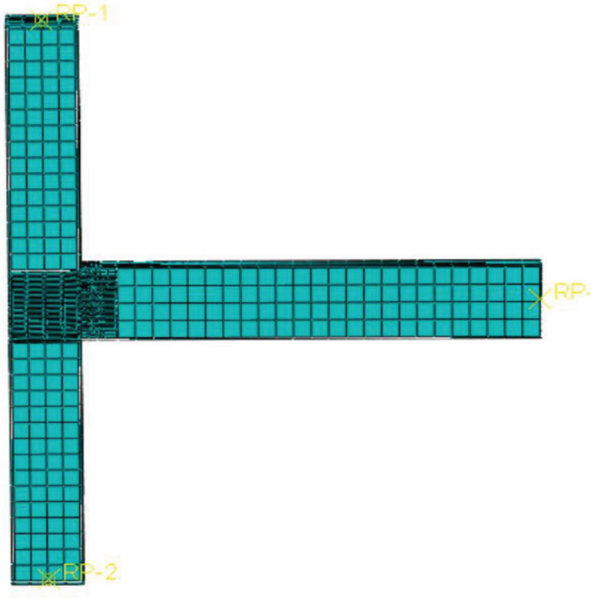

Figure 10. Joint finite element model and mesh division

The concrete damage plasticity (CDP) model was employed to simulate the mechanical behavior of concrete. Research [33] suggests that omitting the damage factor can reduce the computational time significantly; however, this may lead to discrepancies between the computational results and actual values, particularly during the stress-strain decline phase of concrete. The compressive and tensile stress-strain constitutive relationships and damage factors for concrete based on the CDP model were derived in accordance with the Code for Design of Concrete Structures (GB 50010 - 2010) [34], as illustrated in Figure 11. The yield function and flow potential function parameters of the CDP model included a dilation angle of 35°, flow potential eccentricity of 0.15, viscosity parameter of 0.0015, biaxial-to-uniaxial initial yield strength ratio of 1.16, and second stress-invariant ratio on the tension-compression meridian (Kc) of 0.6667. In the simulation, the stress-strain relationships of the reinforcement and steel sections were defined using a bilinear model.

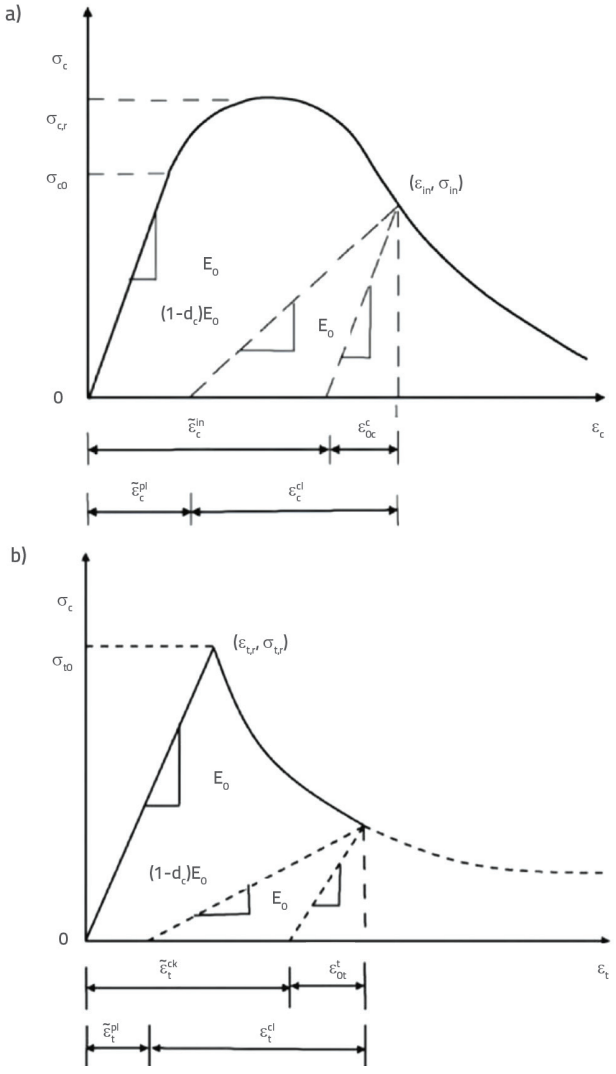

Figure 11. Stress-strain relationship of concrete in CDP model: a) Single-axis compression; b) Single-axis tension

The finite element model employed a paired contact model between the concrete and steel sections, incorporating Coulomb friction with a tangential friction coefficient of 0.5 and adopting a hard contact condition in the normal direction. The flanges were designed to detach outward from the concrete without penetrating inward. In addition, the endpoints of the links were securely attached to the steel beam flanges, whereas the endpoints of the longitudinal reinforcement were connected to the end plates, all of which were embedded within the concrete. The end plates were modeled as rigid bodies with no deformation and were secured via section binding at the termini of the steel beams and concrete.

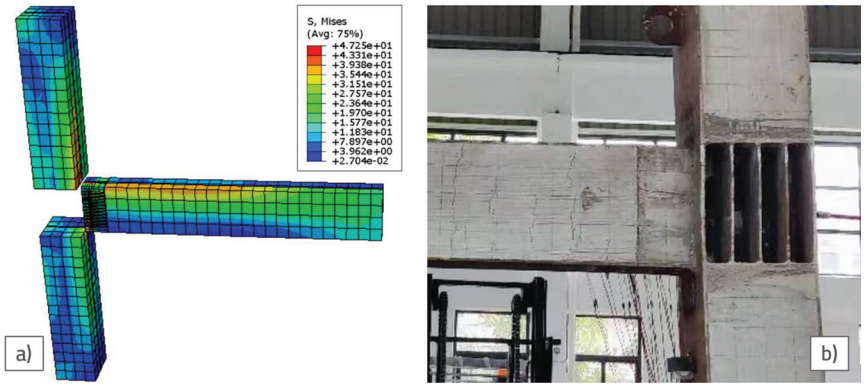

Figure 12. Contrast of concrete failure forms: a) Concrete stress map; b) Actual concrete damage patterns and locations

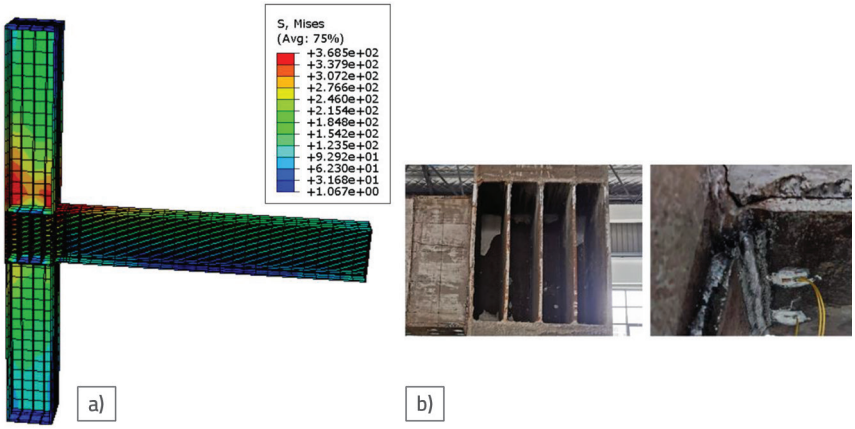

Figure 13. Failure pattern comparison of steel section: a) Concrete stress map; b) Actual concrete damage patterns and locations

4.2. Comparison of numerical simulation and experimental results

4.2.1. Comparative analysis of damage patterns

In ABAQUS, the CDP model prohibits cracking at the integration points, and the direct simulation of element fractures presents significant challenges. Consequently, the cracking and fragmentation of concrete and steel fractures are typically represented by stress contour plots. Figures 12 and 13 illustrate the damage patterns in the concrete and steel, respectively, revealing that the highest stress concentrations occurred at the beam ends within the joint core region. This indicates that bending failure was the dominant failure mode, thereby confirming the accuracy of the finite element model.

4.2.2. Comparative analysis of skeleton curves

Figures 14 and 15 compare the experimentally obtained and finite element simulated hysteresis and skeleton curves, respectively. The selected computational model accurately captured the entire loading process of the PEC beam-column joint, with the load-bearing capacities differing by less than 10 %. Although minor discrepancies in stiffness were observed during the elastic phase and more pronounced differences occurred during the unloading phase of the plastic stage, these variations did not impact the subsequent analyses and demonstrate the strong applicability of the model.

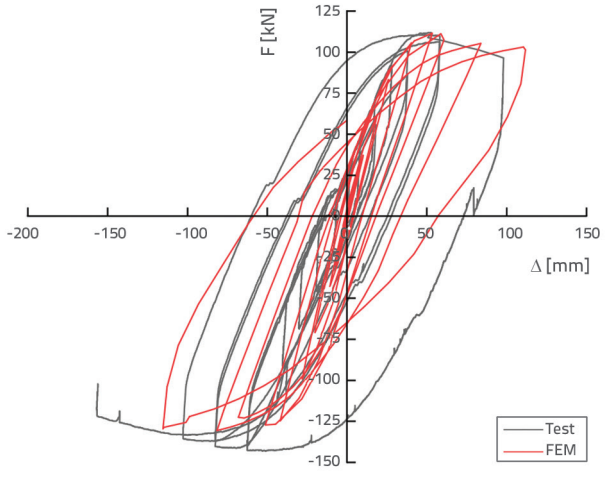

Figure 14. Hysteresis curve comparison

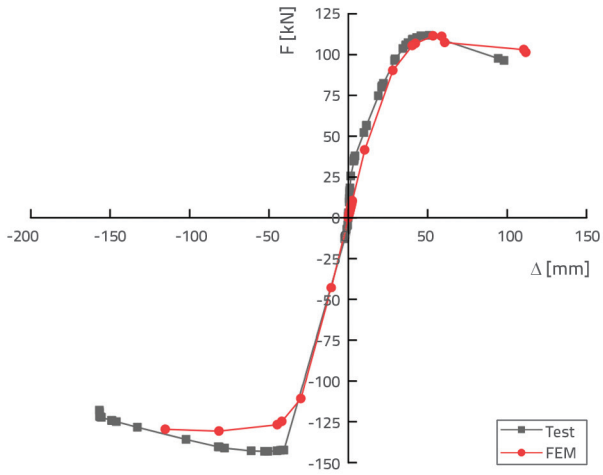

Figure 15. Skeleton curve comparison

4.3. Seismic performance of strong-axis PEC Joints

4.3.1. Analysis of the applicability of local reinforcement schemes

Longitudinal stiffening ribs were introduced into the experimental design as a substitute for the core concrete to address the challenges associated with concrete casting in the core area of the PEC beam-column joint. This modification resulted in bending failures at the beam ends and local buckling of the steel in the core area, which aligned with the design expectations. However, comparative experimental data on specimens incorporating concrete within the joint core area are limited, necessitating further validation of their load-bearing capacities and stiffness.

Building on the previous section, a finite element model was developed for specimen J-1-2, incorporating concrete into the joint core area. Its performance was compared with both the experimental and numerical results for specimen J-1. The hysteresis curve is presented in Figure 16, the skeleton curve in Figure 17, and the stress contour plot in Figure 18.

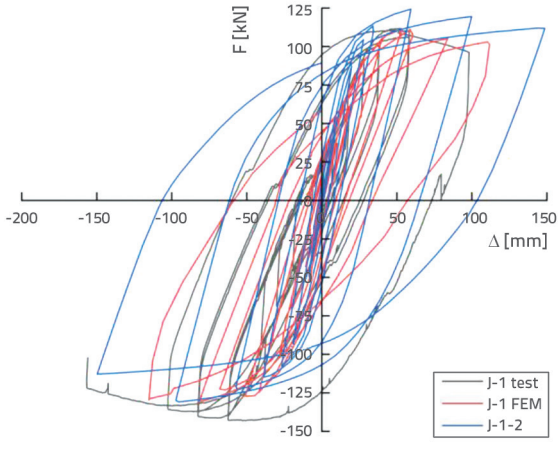

Figure 16. Hysteresis curve comparison

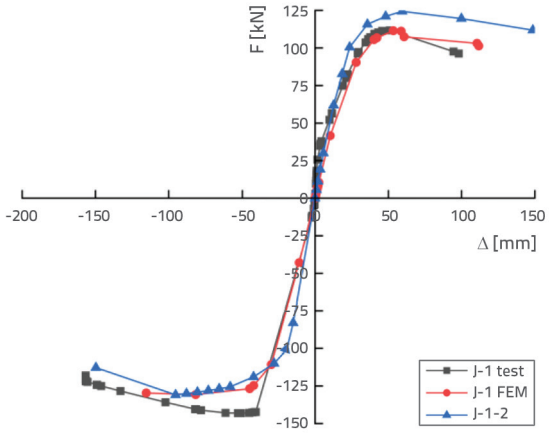

Figure 17. Skeleton curve comparison

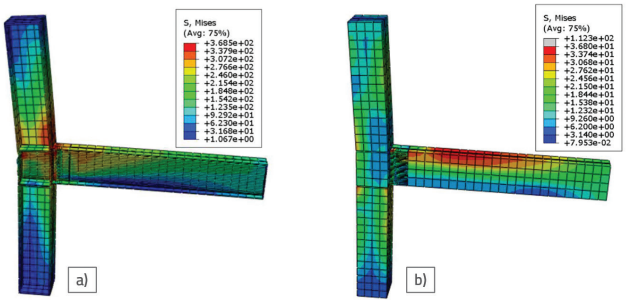

Figure 18. Comparison of hysteresis curves of joints under different levels of dimensionless compressive force

Specimens J-1-2 and J-1 exhibited consistent failure modes that were characterized by bending at the beam ends and local buckling of the primary steel components in the joint core area. Both specimens demonstrated similar load-bearing capacities because ultimate failure consistently occurred at the beam ends, indicating that modifications to the joint area design did not affect the failure location. Specimen J-1-2 exhibited slightly higher stiffness compared with specimen J-1, primarily owing to the longitudinal stiffening ribs, which were designed to have lower stiffness than the filled concrete. This finding suggests that replacing the core area concrete with equivalent longitudinal stiffening ribs provides a viable solution for addressing the casting difficulties in the joint core region.

4.3.2. Influence of different axial pressure ratios

Controlling the axial compression ratio is essential to ensure structural safety and improve seismic performance in seismic design. Design codes typically specify an upper limit for the axial compression ratio to maintain sufficient ductility and load resistance under seismic conditions. Accordingly, finite element simulations were performed on the strong-axis PEC joints with varying axial compression ratios (0.15, 0.30, 0.45, and 0.60). The corresponding hysteresis and skeleton curves are shown in Figures 19 and 20, respectively.

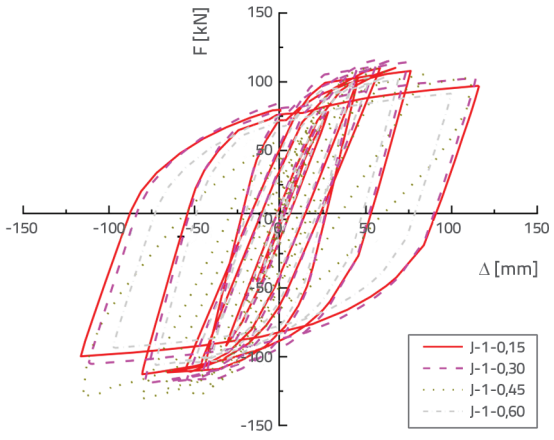

Figure 19. Comparison of hysteresis curves of joints under different coaxial pressure ratios

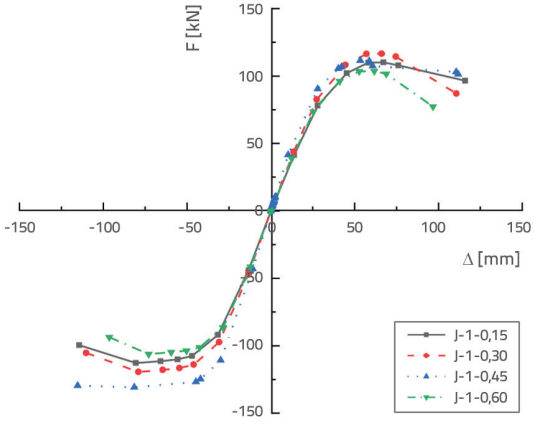

Figure 20. Comparison of skeleton curves of joints under different coaxial pressure ratios

As illustrated in the figures, the overall trends of the hysteresis curves remained consistent across the different axial compression ratios. Initially, the curves covered a relatively small area with minimal variations in stiffness. As the displacement increased, the hysteresis loops expanded into shuttle-like shapes, accompanied by a progressive increase in area and a corresponding decrease in stiffness. As failure approached, the loops retained their shuttle shape but became less pronounced, exhibiting a significant reduction in stiffness. With increasing axial compression ratios, the ultimate and failure load-bearing capacities of the joints initially increased and then decreased, indicating that the axial compression ratio should be carefully optimized in practical design applications.

The equivalent viscous damping coefficient (he) was computed based on the hysteresis loops corresponding to the ultimate and failure loads of the strong-axis PEC joints. The detailed results are presented in Table 4. Both the area enclosed by the hysteresis loops and the equivalent viscous damping coefficient initially increased and then decreased; however, their values remained closely aligned. This trend suggests that the energy absorption capacity of the joints remained relatively stable across the varying axial compression ratios. Notably, as the joints approached failure, the equivalent viscous damping coefficient did not decrease, but instead, exhibited an increasing trend. This finding demonstrates that the strong-axis PEC joints maintained strong energy absorption capabilities, even beyond their ultimate load-bearing capacity.

5. Restoring forces model for strong-axis PEC joints

Building on the finite element analysis presented in Section 4, this section further explores the theoretical aspects of strong-axis PEC joints.

5.1 Skeleton curve model

The skeleton curves of the strong-axis PEC joints under different axial compression ratios were non-dimensionalized, and a three-segment linear skeleton curve model was developed using numerical fitting methods [33, 34]. This model categorizes the curve into three distinct phases: elastic, yield, and load-decreasing segments, as illustrated in Figure 21. The horizontal and vertical axes represent the non-dimensionalized values of the load relative to the maximum positive and negative loads and their corresponding displacements, respectively.

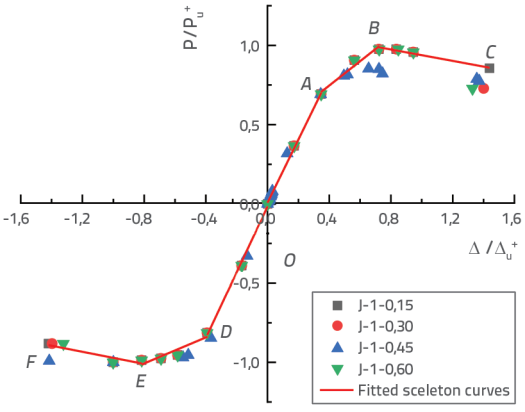

Figure 21. Fitted skeleton curve

Table 4. Energy consumption index of the joints

Axial pressure ratio		Area A [mm²]	h_e		Area A [mm²]	h_e
0.15	Ultimate load capacity	10918	0.21	Destroyed	16984	0.24
0.30		12122	0.23		17427	0.26
0.45		11973	0.23		20314	0.25
0.60		9618	0.22		14212	0.27

Table 5. Skeleton curve model fitting formula

Curved section	Fitted equation	*R2*
BC	*P*/*Pu*+ = 1.99Δ/Δu++0.01	0.99
AB	*P*/*Pu*+ = 0.77Δ/Δu++0.44	0.96
OA	*P*/*Pu*+ = -0.18Δ/Δu++1.12	0.97
OD	*P*/*Pu*+ = 2.07Δ/Δu+-0.02	0.99
OD	*P*/*Pu*+ = 0.41Δ/Δu+-0.68	0.86
EF	*P*/*Pu*+ = -0.19Δ/Δu+-1.16	0.85

The fitting equations for each segment of the skeleton curves of the strong-axis PEC joints are presented in Table 5. All R^2 values exceeded 0.85, indicating a high degree of fitting accuracy. As the PEC joints transitioned into the elastoplastic stage, the unloading stiffness degradation became evident.

5.2. Unloading stiffness

Based on the simulation results of the strong-axis PEC joints under different axial compression ratios, the unloading stiffness at various displacement levels was regressed, yielding Equation (3).

$$\frac{K_1}{K_0} = -0,03\left(\frac{\Delta}{\Delta_u}\right)^3 - 0,45\left(\frac{\Delta}{\Delta_u}\right)^2 + 0,1\left(\frac{\Delta}{\Delta_u}\right) + 1,21 \quad (3)$$

In this equation, K_1 represents the unloading stiffness, K0 denotes the initial stiffness of the joint in the elastic phase, Δ is the applied displacement, and Δ_u corresponds to the displacement at the peak load-bearing capacity of the joint.

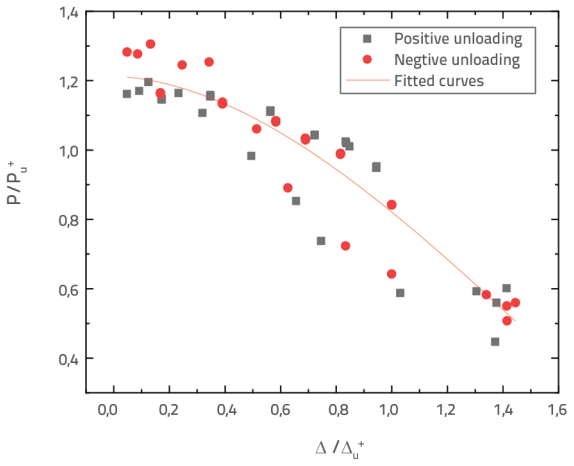

Figure 22. Fitted unloading stiffness curve

Figure 2 compares the scatter plot of the simulation data with the unloading stiffness fitting curve, where the ratio K_1/K_0 follows a cubic function of Δ/Δ_u. The fitting equation yielded an R2 value of 0.87, indicating that Equation (3) provides a high degree of accuracy in predicting the unloading stiffness of strong-axis PEC joints.

5.3. Hysteresis rule

Figure 23 shows the three-segment linear skeleton model of the strong-axis PEC joint, which is described as follows.

- Elastic stage: During phase, loading and unloading occurred along the initial stiffness K_0.
- Elastoplastic stage: Upon reaching yield point A, the joint transitioned into the elastoplastic phase and continued loading to yield point B with stiffness K_{AB}.

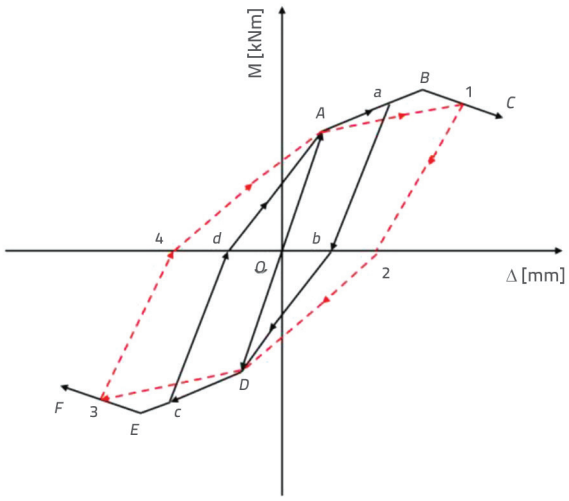

Figure 23. Restoring force model of strong-axis PEC joints

Starting from unloading point a, the unloading followed the path derived in Section 4.2. From point b, reverse loading proceeded along path b-D-c to point c. From point c, unloading occurred along the unloading stiffness path towards point d, followed by forward loading back to yield point A. (3) Hysteresis cycle: This cycle was repeated, where forward loading progressed from point B to point C, followed by unloading from forward unloading point 1 along the unloading stiffness path. Reverse loading then occurred from unloading point 2 to yield point D and

proceeded towards point 3. From reverse loading point 3, the unloading followed the unloading stiffness path towards point 4. Finally, forward loading resumed to yield point A and returned to point 1.

5.4. Validation of restoring force model

A comparison between the hysteresis curves derived from the theoretical skeleton model and experimental results for specimen J-1 is shown in Figure 24. Across the elastic and elastoplastic stages, the computed hysteresis curves exhibited a strong correlation with the experimental data, confirming that the restoring force model effectively supports the elastoplastic seismic response analysis of strong-axis PEC joints.

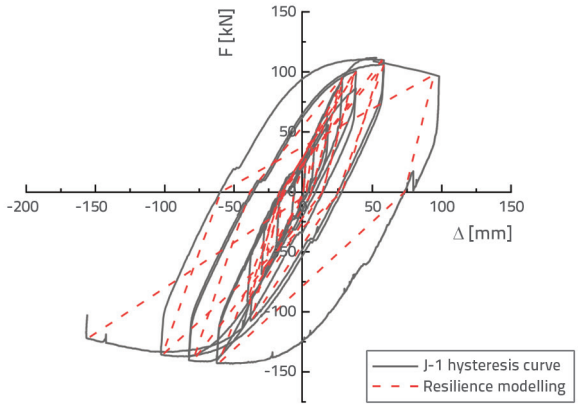

Figure 24. Comparison between calculation of restoring force model and test results

6. Conclusions

Based on the experimental study and finite element parameter analysis of the PEC joints, the following conclusions were drawn:

- Failure of the strong-axis PEC joints occurred primarily at the beam ends, with only minor deformations observed in the core area. The ductility factor exceeded 3, indicating strong energy absorption capabilities and excellent seismic performance.
- Both the experimental and finite element analyses confirmed that replacing the core concrete with equivalent longitudinal stiffening ribs is a viable solution for addressing the challenges associated with concrete casting in the core area.
- As the axial compression ratio increased, the load-bearing capacity of the strong-axis PEC joints initially increased and then decreased, whereas the variations in the energy absorption capacity remained minimal.
- A restoring force model for strong-axis PEC joints was developed and validated, and the simulation results closely matched the experimental results. This model provides a reliable tool for analyzing the elastoplastic seismic response of strong-axis PEC joints.

Acknowledgements

The authors thank Hongxin Liu and Yaming Li for their contributions to the conceptualization, methodology, and funding acquisition of the research. Shuizhong Jia is acknowledged for writing the original draft, and Xiaomeng Xie is recognized for their contributions to writing, reviewing, and editing. The authors also thank Yukun Yang from Shanghai Jieyi Construction Technology Co., Ltd., and Jie Li from Sanda University and Tongji University for their valuable contributions to this research, despite not being listed as authors. Their efforts in the methodology and software development were instrumental in completing this study.
This research was supported by the Scientific Research Project of the Shanghai Science and Technology Commission (21DZ1203002) and the East China Construction Group Co., Ltd. (Class 20-1-0073-Junction).

REFERENCES

[1] Fischinger, M., Kramar, M., Isaković, T.: Seismic safety of prefabricated reinforced-concrete halls-analytical study, Građevinar, 11 (2009), pp. 1039-1045. https://hrcak.srce.hr/43827

[2] Du, H., Hu, X., Shi, D., et al.: Effect of reinforcement on the strength of the web opening in steel-concrete composite beam, Engineering Structures, 235 (2021), Paper 112038, https://doi.org/10.1016/j.engstruct.2021.112038

[3] Ji, G., Zhu, E., Wang, B., et al.: Bearing capacity analysis of perfobond rib shear connectors in steel-concrete composite structures, Structures, 57 (2023), Paper 105292, https://doi.org/10.1016/j.istruc.2023.105292

[4] Kindmann, R., Bergmann, R., Cajot, L.G., et al.: Effect of reinforced concrete between the flanges of the steel profile of partially encased composite beams, Journal of Constructional Steel Research, 27 (1993) 1-3, pp. 107-122, https://doi.org/10.1016/0143-974X(93)90009-H

[5] Hao, N., Yang, Y., Xue, Y., et al.: Shear performance of partially encased composite beams with high-strength steel and UHPC, Journal of Constructional Steel Research, 211 (2023), Paper 108217, https://doi.org/10.1016/j.jcsr.2023.108217

[6] Xue, Y., Hao, N., Yang, Y., et al.: A novel shear strength model for partially encased composite (PEC) beams based on strain compatibility, Engineering Structures, 267 (2022), Paper 114660, https://doi.org/10.1016/j.engstruct.2022.114660

[7] Song, Y.C., Wang, R.P., Li, J.: Local and post-local buckling behavior of welded steel shapes in partially encased composite columns, Thin-Walled Structures, 108 (2016) 11, pp. 93-108, https://doi.org/10.1016/j.tws.2016.08.003

[8] Qian, Z., Wang, J., Liu Y., et al.: Axial compressive performance of partially encased steel-concrete composite stub columns filled with lightweight aggregate concrete, Engineering Structures, 291 (2023), Paper 116422, https://doi.org/10.1016/j.engstruct.2023.116422

[9] Wang, N., Hou, H., Wang, Y., et al.: Flexural behavior of partially encased cellular beams: tests and design implications, Engineering Structures, 293 (2023), Paper 116631, https://doi.org/10.1016/j.engstruct.2023.116631

[10] Zhao, B., Huo, H., Ran, C., et al.: Flexural behavior of castellated partially encased composite (PEC) beams, Journal of Constructional Steel Research, 214 (2024), Paper 108509, https://doi.org/10.1016/j.jcsr.2024.108509

[11] Zhan, X., Qin, Z., Li, J., et al.: Global stability of axially loaded partially encased composite column with L-shaped section, Journal of Constructional Steel Research, 200 (2023), Paper 107671, https://doi.org/10.1016/j.jcsr.2022.107671

[12] Wang, W., Cai, H., Bai, C., et al.: Seismic performance of partially encased concrete composite columns with corrugated web, Journal of Building Engineering, 77 (2023), Paper 107481, https://doi.org/10.1016/j.jobe.2023.107481

[13] Marimuthu, S., Sivasankara, Pillai, G.: Experimental investigation of exterior reinforced concrete beam-column joints strengthened with hybrid FRP laminates, Građevinar, 73 (2021) 4, pp. 365-379, https://doi.org/10.14256/JCE.2765.2019

[14] Coşgun, T., Coşgun, C., Kaniskha, A., et al.: Seismic load tests on exterior beam-column connections of existing RC structures, Gradevinar, 71 (2019) 12, pp. 1129-1141, https://doi.org/10.14256/JCE.2524.2018

[15] Pekgökgöz, R.K., Avcil, F.: Effect of steel fibres on reinforced concrete beam-column joints under reversed cyclic loading, Građevinar, 73 (2021) 12, pp. 1185-1194, https://doi.org/10.14256/JCE.3092.2020

[16] Spavier, P.T., El Debs, A.L.H.C.: Experimental analysis of beam-to-column connection with partially encased concrete column with varying inertia axis, Journal of Constructional Steel Research, 194 (2022), Paper 107325, https://doi.org/10.1016/j.jcsr.2022.107325

[17] Chen, C.C., Sudibyo, T., Erwin: Behavior of partially concrete-encased steel beams under cyclic loading, International Journal of Steel Structures, 19 (2019), pp. 255-268, https://doi.org/10.1007/s13296-018-0114-y

[18] Wang, J., Hu, Z., Guo, L., et al.: Analytical performance and design of CECFST column assembled to PEC beam joint, KSCE Journal of Civil Engineering, 25 (2021), pp. 2567-2586, https://doi.org/10.1007/s12205-021-1055-0

[19] Huang, H., Chen, Z., Lu, Y., et al.: Experimental study on seismic performance of frame with steel-hollow core partially encased composite spliced beam, Journal of Constructional Steel Research, 212 (2024), Paper 108239, https://doi.org/10.1016/j.jcsr.2023.108239

[20] Huang, H., Yao, Y., Liang, C., et al.: Experimental study on cyclic performance of steel-hollow core partially encased composite spliced frame beam, Soil Dynamics and Earthquake Engineering, 163 (2022), Paper 107499, https://doi.org/10.1016/j.soildyn.2022.107499

[21] Yu, J., Zhao, C., Zhong, W.: Seismic behavior of partially encased composite columns-steel plate shear wall structure with different semi-rigid joints, Journal of Building Engineering, 82 (2024), Paper 108177, https://doi.org/10.1016/j.jobe.2023.108177

[22] Li, W., Fan, H.T., Jiang, H.M., et al.: Seismic Behavior of Demountable Reinforced Concrete (RC) Beam-to-Column Joints with Damage-Control Fuses, Buildings, 14 (2023) 1, Paper 20, https://doi.org/10.3390/buildings14010020

[23] Dang, B., Li T., Wang, S., et al.: Design method and engineering application of shear wall with friction energy dissipation damper, Građevinar, 74 (2022) 4, pp. 277-289, https://doi.org/10.14256/jce.2742.2019

[24] Zhao, C., Gao, S., Zhao, G., et al.: Model test research on restoring force of joints in partially wrapped concrete pillar-shaped steel beam frame, Architectural Structure, 5 (2023) S1, pp. 1818-1824 (in Chinese).

[25] Li, Y., Fan, M., Song, H., et al.: Restoring force model of a modular steel-concrete composite column, Case Studies in Construction Materials, 20 (2024), Paper e03128, https://doi.org/10.1016/j.cscm.2024.e03128

[26] Zhuang, M.L., Sun, C., Bai, L., et al.: A restoring force model for a novel type of precast beam-to-column joints using mechanical connections, Case Studies in Construction Materials, 18 (2023), Paper e01840, https://doi.org/10.1016/j.cscm.2023.e01840

[27] Wu, C.L., Liu, X., Pan, W., et al.: Restoring force model for modular prefabricated steel-reinforced concrete column to H-shaped steel beam composite joints, Journal of Building Engineering, 42 (2021), Paper 102845, https://doi.org/10.1016/j.jobe.2021.102845

[28] Dai, K.Y., Yu, X.H., Lu, D.G.: Phenomenological hysteretic model for corroded RC columns, Engineering Structures, 210 (2020), Paper 110315, https://doi.org/10.1016/j.engstruct.2020.110315

[29] Bian, J., Cao, W., Zhang, Z., et al.: Cyclic loading tests of thin-walled square steel tube beam-column joint with different joint details, Structures, 25 (2020), pp. 386-397, https://doi.org/10.1016/j.istruc.2020.03.027

[30] Test method standard for physical and mechanical properties of concrete: GB/T 50081-2019, Standards Press of China, 2019 (in Chinese).

[31] Tensile test method for metal materials at room temperature: GB/T 228-2002, Standards Press of China, 2002 (in Chinese).

[32] Code of seismic test methods for buildings: JGJ 101-1996, China Academy of Building Research, 1996 (in Chinese).

[33] Chang, X., Wang, X., Liu, C., Wu, Z.: Reliability evaluation of finite element model for flexural performance of RC beams reinforced by Prestressed FRP plates, Journal of Nanjing University of Technology (Natural Science Edition), 43 (2021) 3, pp. 318-328 (in Chinese).

[34] Wang, W., Zhang, J., Yin, X., Liu, J.: Seismic analysis of partial encased composite beam-column joints considering design factors, Journal of Building Engineering, 28 (2021), Paper 101093 (in Chinese).